

Pictor A (PKS 0518–45) - From Nucleus to Lobes

S. M. Simkin^{1,2,3}

Michigan State University, East Lansing, MI 48824-1116

E. M. Sadler^{1,3}

School of Physics, University of Sydney, NSW 2006, Australia

R. Sault³

Australia Telescope National Facility, CSIRO, Epping, NSW 1710 Australia

S. J. Tingay

California Institute of Technology, Jet Propulsion Laboratory (MS238-332), 4800 Oak Grove Drive, Pasadena, CA 91109

and

J. Callcut⁴

Michigan State University, East Lansing, MI 48824-1116

ABSTRACT

We present a variety of new imaging and kinematic data for the double-lobed radio galaxy Pictor A. The new optical data include HST continuum and [OIII], emission-line images (at a resolution of 25 – 100 mas) and ground-based imaging and spectroscopy (at a resolution of $\sim 1.5''$). The ground-based images show H α filaments and loops which extend to the N and W of the optical core. The radio continuum data include 3 cm Australia Telescope images of the core, at a resolution comparable to that of the optical, ground-based images, and a VLBI image of a jet in the compact core (at a resolution of 2 – 25 mas), which seems to align with a continuum “jet” found in the HST images. The core radio jet, the HST optical continuum “jet”, and the NW H α filaments all appear to be aligned with the extended, low luminosity radio continuum bridge which Perley et al. 1997 have traced out to the optical-synchrotron hot-spot in the NW lobe of this object. The H α filaments which appear to lie in the path of

¹Visiting Astronomer, Cerro Tololo Inter-American Observatory. CTIO is operated by AURA, Inc. under contract to the National Science Foundation.

²Visiting Astronomer, Space Telescope Science Institute, STScI is operated by AURA, Inc. under contract to NASA

³Visiting Astronomer, The Australia Telescope, funded by the Commonwealth of Australia for operation as a National Facility managed by CSI

⁴NSF REU summer student, 1992

this trajectory are associated with a disrupted velocity field in the extended ionized gas. These filaments (as well as the extended [OIII] emission found at mas scales in the HST images) may have been pushed to the N, out of the path of the jet. The ground-based spectra which cover this trajectory also yield line ratios for the ionized gas which have anomalously low [NII] (6564), suggesting either a complex, clumpy structure in the gas with a higher cloud-covering factor at larger radii and with denser clouds than is found in the nuclear regions of most NLRG and Seyfert 2 galaxies, or some other, unmodeled, mechanism for the emergent spectrum from this region. The H α emission-line filaments to the N appear to be associated with a 3 cm radio continuum knot which lies in a *gap* in the filaments $\sim 4''$ from the nucleus. Altogether, the data in this paper provide good circumstantial evidence for non-disruptive redirection of a radio jet by interstellar gas clouds in the host galaxy.

Subject headings: radio continuum: galaxies — galaxies: jets — galaxies: kinematics and dynamics — galaxies: individual (Pictor A)

1. Introduction

1.1. Background

Pictor A is the closest, double-lobed radio source with a well-defined jet and an active, optical-synchrotron hot-spot (Meisenheimer and Röser 1987, Thomson et al. 1995). Recent, high-resolution, multi-frequency VLA radio images find a “bridge” or channel of low-level radio emission which links this hot-spot to the nuclear region (Perley et al. 1997). It is the seventh brightest radio source in the sky at 408 MHz and the most powerful radio galaxy in the redshift range $0 < z < 0.04$. It is also the nearest broad-lined radio galaxy with a nuclear, optical spectrum which has broad, permitted emission lines (H, He), and relatively narrow optical forbidden emission lines ([OI], [SII], [OIII], [NII]) superimposed on a featureless continuum. The broad permitted lines have $FWOI > 14,000 \text{ km s}^{-1}$ (from our CTIO measurements reported in this paper), but are reported to be as high as $23,000 \text{ km s}^{-1}$ (Filippenko 1985, Sulentic et al. 1995, Halpern et al. 1996 and references therein), with a highly excited nuclear spectrum. It has a compact radio core (Christiansen et al. 1977). Its redshift is $z = 0.035$ ($v = 10,500 \text{ km s}^{-1}$), giving a distance, $D = 110 \text{ Mpc}$, if $H_0 = 100 \text{ km s}^{-1} \text{ Mpc}^{-1}$ and $q_0 = 0$. All distance-dependent values in this paper have been scaled to $H_0=100$ with the appropriate scaling factor, $h=10^{-2}H_0$. (With this value of H_0 , the physical scale for Pictor A is roughly $530 \text{ pc}(\text{''})^{-1}h^{-1}$.)

1.2. Extended Optical Structure (EELG)

This object has been identified as one of a class of double-lobed radio galaxies which contain extensive regions of non-nuclear, ionized gas (cf. Carswell 1984, Robinson 1987, Baum and Heckman 1989a, Baum and Heckman 1989b and references therein.) This extended, ionized gas (EELG) is known to have a peculiar, apparently non-rotational, velocity field (Tadhunter et al. 1989). The extended emission-line gas has been imaged at low resolution and with low signal-to-noise in the redshifted emission lines of both $H\alpha$ -[NII] and [OIII]- $\lambda 5007$ as well as continuum emission (Hansen et al. 1987, Fraix-Burnet et al. 1991.)

There are now several examples of nearby Seyfert galaxies with well-studied, non-nuclear, extended emission line regions (Allen et al. 1998 and references therein). There are also several studies of the

EELG associated with extended radio emission for intermediate redshift radio galaxies (Villar-Martin et al. 1998, Allen et al. 1998 and references therein). There are, however, very few nearby, powerful, double-lobed radio galaxies (FR II objects) and thus extensive studies of this type of object are lacking.

1.3. Motivation for the Present Study

FR II galaxies are important because they represent one extreme edge of the phenomenological envelope which defines “active galaxies.” They are rare because the radio-loud fraction of the AGN population is small. Thus the opportunity to study such an object with high spatial resolution is also rare. Because it is both nearby and an extreme example of a powerful, almost quasar-like, radio galaxy, we regard Pictor A as an excellent, natural laboratory for identifying those features which differentiate radio-loud AGN from their radio-quiet counterparts and for studying the structure of the beamed radio plasma which produces the strong radio hotspots seen in FR II sources. In this paper we combine a wide variety of different observations in an effort to elucidate the relationship between the jet, lobes, and peculiar optical structure and kinematics in this galaxy. We believe that this type of approach, where diverse observations are analyzed and critically examined in one body of work, can lead to a much better understanding of the interrelationships between these different characteristics than a more piecemeal approach.

We began our study of this object as part of a program to obtain detailed measurements of the velocity fields in FR II radio galaxies with extended ionized gas. Although initial observations of several such objects suggested a simple relationship between internal, rotational kinematics and the axis of radio emission (Simkin 1979, it became clear that the situation was much more complex (cf. the discussions in Heckman et al. 1985 and Baum and Heckman 1989b) and warranted a program of extensive mapping of the velocity fields in several well-resolved objects. Our new study, which included narrowband, optical imaging (section 2.1) and spectroscopy (section 2.3), evolved into a much more extensive one which included HST imaging (section 3) and, finally, radio imaging (sections 2.2 and 4.4).

For the sake of brevity, we have attempted to limit our discussion of observational reduction techniques in this paper (although they are critical to understanding the limitations of the present data), referring

to other published (or soon to be published) sources where possible. The one exception to this limited discussion of the data analysis is our treatment of the HST image reduction in Section 3.3. This analysis is unique and cannot be replicated unless and until the HST is again equipped with a camera and filters which can be used for redshifted, emission-line imaging of this object.

In the final analysis, the goal of this study is to identify which measurable, physical parameters are critical for understanding the radio galaxy phenomenon. Once identified, these can be incorporated into more focused observational surveys covering a more complete sample, which will allow a more general understanding of the physical basis for the type of extreme radio activity seen in classical FR II radio galaxies.

2. Ground-Based Observations (CTIO and ATCA)

2.1. Direct Optical Images (Continuum and H α)

Direct images of Pictor A were taken in February 1987 with the CTIO 1.5m, 800 \times 800 TI CCD and $f/7.5$ cassegrain secondary. The CCD scale was 0.27 "pixel⁻¹. The telescope PSF showed evidence of coma (due to mis-alignment of the secondary) but the image cores were well-defined.

Imaging was done through two interference filters, $\lambda 6560$ ($\Delta\lambda 110\text{\AA}$), covering the continuum, and $\lambda 6826$ ($\Delta\lambda 78\text{\AA}$), covering redshifted [SII]-H α -[NII]. We used the narrow band $\lambda 6560$ filter to obtain continuum observations because it provides a better match for the $\lambda 6826$ filter in terms of PSF formation and exposure effects than a broad-band filter. The $\lambda 6560$ filter does, however, include the redshifted [OI] $\lambda 6364$ emission line at 6587\AA , which appears to extend beyond the nucleus. However, this should introduce minimal distortion of the H α image (if any) since even in the nucleus the strength of the [OI] $\lambda 6364$ line is less than 7.5% of that from H α (table 3). The imaging observations are listed in table 1.

The images were reduced using the "IRAF" package in the standard way (correcting for detector response by removing biases, dark current, and normalizing with "dome" flats). The reductions for the entire set of CTIO images are described in more detail in Grimberg et al. 1999. The H α images were corrected for continuum flux by normalizing the stellar images

in the $\lambda 6560$ filter to the same relative flux as those in the $\lambda 6826$ filter and then subtracting. The continuum and corrected H α images are shown in Figure 1a (continuum isophotes) and 1b (H α grayscale). The H α image shows a wealth of arc-like, detailed structure in the ionized gas throughout the inner 3" to 8" (1.6 to 4.5 h^{-1} kpc) of the nucleus. Although several nearby radio galaxy hosts show organized, arc-like structure in their extended ionized gas (cf. PKS0634-20 and 3C227 in Hansen et al. 1987, Baum et al. 1988 and Prieto et al. 1993), none show such a large, complete loop such as this.

Three points are noteworthy:

1. *Offset in the Continuum Image:* The $\lambda 6560$ \AA continuum image (Figure 1a) has a much steeper profile toward the S than the N. As we will see in section 2.2, this offset may well be related to an important new feature which we have identified in the 3 cm radio image.
2. *H α Pseudo-Ring to the N:* The H α image (Figure 1b) shows a loop of emission reaching 4" to the N with a gap at PA -15° . This was seen in the much lower resolution image of Hansen et al. 1987 as two low-luminosity "horns" on either side of the central image. Here it is clearly reminiscent of the types of rings, or "pseudo" rings, seen in some barred spirals and Seyfert galaxies (Su and Simkin 1980.) Again, as we will see in section 2.2, it may be intimately related to an unusual 3 cm radio continuum feature.
3. *H α Bridge to the WNW:* There is also an open arc or bridge extending to the W in the H α image (Figure 1b). This feature (at PA 283°) ends in a knot at $\sim 7.8''$ from the nucleus. (This seems to have first been seen in spectra by Baldwin and Compusano as reported in Carswell 1984 and, with hindsight, appears in the lower resolution in the image by Hansen et al. 1987.)

The relationship of these optical features to the radio continuum emission is shown in figures 2 and 3. In Figure 2, the 20 cm VLA, radio image of Perley et al. 1997 (resolution 7.5") is displayed with a scale which shows the bridge linking the nucleus to the NW radio hot-spot. The inset in Figure 2 shows isophotes from the H α image in Figure 1b with the direction of the NW hot-spot (at PA $280-281^\circ$) and the counter direction of the SE hot-spot (at PA $288-289^\circ$) shown

by the arrows. The H α extension at PA 283 $^\circ$ as well as the 20 cm radio bridge are both *nearly* aligned with the direction of the hotspots.

The relationship between the N H α pseudo-ring and the radio continuum is discussed below:

2.2. Radio imaging (ATCA)

Pictor A has no discernible optical continuum jet on arcsecond scales (Fraix-Burnet et al. 1991), and although the 20 cm observations of Perley et al. 1997, plotted in Figure 2, show a kpc-scale jet pointing to the nucleus from the NW hot-spot, they do not reveal a small-scale jet. However, the H α feature shown in Figure 2 and the continuum feature seen in our HST Cycle 1 observations (section 3) are so well aligned with the 130 kpc-distant, NW hotspot that we made three 12-hour 3 cm synthesis observations with the Australia Telescope Compact Array (ATCA) to search for radio continuum features which might correlate with the optical features we found in the CTIO and HST data.

2.2.1. Observations

The ATCA is an east-west, 6-antenna, interferometer array located in south-eastern Australia (Australia Telescope 1992). Three array configurations were used (the so-called 6A, 6C and 6D configurations), which give good Fourier plane coverage out to 6 km. The observations were on 1993 Jan 10, 1993 Feb 11 and 1993 Sep 20. A fourth configuration was rendered unusable by an error in the on-line system. The flux scale was set using PKS1934-638 (Reynolds 1994), whereas PKS0534-340 was used as the phase calibrator. The technique of multi-frequency synthesis (Conway et al. 1990, Sault 1994) was used to improve the Fourier plane coverage beyond that which would normally be achieved with the available configurations. Multi-frequency synthesis relies on measuring different Fourier spacings by varying the observing frequency. In each observing run, we alternated between two setups every 5 min, with each setup observing two different frequencies simultaneously (i.e. in each run, we observed four distinct frequencies). The observing frequencies were in the range 8.24 to 9.11 GHz, with the weighted mean being 8.62 GHz.

2.2.2. Reductions and Analysis

The data were flagged and calibrated in the Miriad system (Sault 1995), with each frequency calibrated

separately. Images were formed, deconvolved and self-calibrated in a fashion similar to that used by Sault 1994. This procedure determines and corrects for the effects of non-zero spectral indices in multi-frequency synthesis. The shortest spacing used in the imaging was 153 m, which resolves out the very extended emission seen by Perley et al. 1997.

The resultant images have moderate dynamic range in the region of the core (1:2000), which is worse than the thermal limit by a factor of 6. The limit in the reconstruction is believed to be related to the size of the object. The north-east hot-spot occurs well out in the primary beam (the north-east hot-spot is 250 arcmin from the core, whereas the half-width at half-maximum of the primary beam response is about 176 arcmin). Deviations from the primary beam response being circularly symmetric this far out, as well as possible pointing problems, have resulted in the imaging of the north-east hot-spots being quite poor (Figure 3.)

We searched for but found no evidence for variation of the flux density of the core (0.92 Jy at 8.62 GHz) over the 8-month period of our observations.

2.2.3. Radio Images

The resulting 3 cm radio map is shown in Figure 3. The inset to Figure 3 shows the core of this image plotted on top of the gray-scale H α image shown in Figure 1b. The radio-optical images have been registered so that the peak optical (nuclear) brightness corresponds to the measured peak in the radio core. This introduces an offset of $\alpha=0.4''$ and $\delta=-1.4''$ (optical - radio). This is well within the accuracy of the HST-GSC 1.0 optical position (Lasker et al. 1990, Jenkner et al. 1990, Russell et al. 1990). With this offset, we note a lobe (located at PA = -15 $^\circ$ and 4'' N of the core) *the peak of which is coincident with the gap in the H α loop at that position* (Figure 3-inset). Although this lobe is weak (it is weaker than some of the artifacts in the north-east and south-west hot-spots), its peak is ten times the rms in the vicinity of the core, it appears in images made from the three configurations individually, and it is robust to various self-calibration models. Hence we believe this lobe is not an artifact.

2.3. CTIO spectra

Nine long-slit spectra were taken during four consecutive nights in February 1987 with the CTIO 4m

spectrograph and the TI CCD. Two additional spectra were taken with the same instrument in January 1988. All exposures were bracketed with spectra of a HeArNe arc lamp taken with the spectrograph in the same PA as the galaxy spectrum and the telescope at the sky positions corresponding to the start and end positions for the intervening galaxy spectrum. The slit positions and observing details are shown in table 2. In all cases the scale along the slit was $0.73''/\text{pixel}$; The slit width was $180\ \mu\text{m}$ ($1.2''$). All galaxy exposures were 2000 seconds.

2.3.1. Calibration

The spectra were flat-fielded, calibrated in wavelength using the arc spectra, and “scrunched” to remove S-distortion. The internal consistency in the fits to the calibration data was $\pm 0.37\text{\AA}$ for the blue-green spectra and $\pm 0.30\text{\AA}$ for the red spectra. The final dispersions were $1.49\text{\AA pixel}^{-1}$ and $1.21\text{\AA pixel}^{-1}$ respectively. The calibrated spectra were used to measure wavelength positions for the emission lines $\text{H}\alpha$, β , $[\text{O I}]$, $[\text{O III}]$, $[\text{N II}]$, and $[\text{S II}]$. These were then used to calculate absolute velocities at each position (stepping $0.73''$) from the nucleus where the observed emission lines were at least 3 times the estimated “noise” in the adjacent continuum. The internal error estimates noted above yield a formal error for the velocity determinations of 14 km s^{-1} for the red emission lines and 21 km s^{-1} for the blue. Since these do not include systematic effects, one might expect these estimates to define a lower limit to the velocity measurements. However, the average nuclear velocity from all of the measurements is $10548 \pm 21\text{ km s}^{-1}$ (section 2.3.2), suggesting that the CTIO spectrograph was quite stable over the 13 month period when the observations were taken. (We note that this *internal* accuracy does not measure any *systematic* shifts in the velocity zero points.)

Although we observed flux calibration standards for all of these spectra, it is clear from examination and comparison of these calibration spectra from night to night that the nights were non-photometric, with flux variations of a factor of 2 or 3 from one night to the next and up to 1.5 on the same night⁵. Thus it is not possible to obtain meaningful absolute

⁵We note that a spectrum of the nuclear region in Pictor A which we loaned for the purpose of measuring line widths has been published with this faulty calibration and should be disregarded in any absolute comparisons - see Sulentic et al. 1995.

values for the emission line strengths nor is it possible to obtain meaningful flux ratios for emission lines, such as $[\text{O I}]\lambda 6300$ and $[\text{O III}]\lambda 5007$, which were taken with different grating settings on different nights. We have, however, determined the *relative* corrections to the ratios, using the published absolute flux values for the stars observed. Even in the most extreme case of $[\text{O I}]/\text{H}\alpha$ these are less than ± 0.04 in the log. A more detailed discussion of the spectral measurement and calibration techniques used for the entire set of CTIO spectra can be found in (Grimberg et al. 1999).

2.3.2. Velocity Analysis

The velocity-position data from different emission lines in the same PA were combined and fit with a spline curve. This spline fitting technique gives 1) a mean central redshift of $10548 \pm 21\text{ km s}^{-1}$ and 2) rms deviations from the fitted curves at any one position angle which range between 22 and 25 km s^{-1} . There are some cases in the literature where the nuclear velocities for AGNs obtained from $[\text{O III}](\lambda\lambda 4958/5007)$ are systematically blueshifted with respect to those obtained from measurement of other optical emission lines (Mackenty et al. 1994, Wilson and Baldwin 1985). However, the consistency between the rms errors for the nuclear velocity from different position angles, and the errors obtained from the spline fits at any one position angle, suggest that this is not a significant factor for Pictor A. Figure 4 (a-h) shows the original velocity measurements for each PA plotted on the right hand side and the resulting composite curves, zeroed to the nuclear velocities, on the left.

Although the velocity curves in Figure 4 appear to show a rotational trend in the ionized gas (receding most rapidly toward the NE and approaching in the SW), the sharp excursions from this trend are as notable as the trend itself. In particular, the velocities in PA 90° , 102° , and 115° have a wave-like appearance with an amplitude of 50 to 100 km s^{-1} (also seen in PA 290° , Robinson 1987.) To help clarify these peculiar velocities, we have constructed a “velocity map” of the ionized gas in the inner regions of Pictor A. Figure 5a shows the spectrograph slit positions projected onto the optical continuum image of the galaxy. Since the slit widths ($1.2''$) and the separation between pixel columns ($0.73''$) were less than the effective seeing profile ($\sim 1.4''$ FWHM), adjacent positions in a map of the velocity plotted on the sky for each slit position contain correlated velocity information. The spline fits to the emission line veloci-

ties for different position angles were used to generate such a two-dimensional “velocity map” of the ionized gas. In areas where the slit positions were within the region of overlapping seeing, this redundant information was used to interpolate points in the “map.”

The result is shown in Figure 5b. There, negative velocities are shown as dashed contours (ranging from -70 km s^{-1} to -10 km s^{-1} in steps of 15 km s^{-1}) and positive velocities are shown as solid contours (ranging from $+10 \text{ km s}^{-1}$ to $+100 \text{ km s}^{-1}$, again in steps of 15 km s^{-1}). The technique used does smooth the velocities in the map, but by what appears to be no more than $\sim 15 \text{ km s}^{-1}$. The gaps in the velocity information for PA 15° – 30° , 60° – 90° and 128° – 180° are apparent. However, the general trend seen in the individual line plots is clear. 1) There appears to be a null, or projected rotation axis at $\sim 120^\circ$ – 140° 2) There is a redshifted velocity plume on the *blueshifted side* of this null region, roughly 1.5 – $2.5''$ to the W of the nucleus (in a cone between PA $\sim 270^\circ$ and $\sim 290^\circ$, marked as $+45 \text{ km s}^{-1}$). This is the feature which shows up so strongly in the individual velocity curves for PA 90° , 102° and 115° (Figure 4e–g) and (from those individual plots, where smoothing is less important) has an amplitude in excess of 60 km s^{-1} in PA 102° .

2.3.3. Analysis of Emission Line Intensities

1. *The Gas Along the Velocity Plume:* To investigate the physical conditions in the gas which gives rise to the redshifted velocity feature on the W side of the nucleus, we measured the relative intensities of the *narrow part* of the emission lines from the spectra in PA 90° , 112.5° , 115° and 128° . The region of interest lies between $1''$ and $2.5''$ from the nucleus in each of these position angles and covers 3 to 4 columns in the ccd images. Figure 6 shows a plot of the relative flux from the nucleus for the red spectrum in PA 102° and the region around the $\text{H}\alpha$ line from the nucleus and 3 ccd columns towards the W. As noted above, the space between columns is less than the FWHM of the seeing profile, and these spectra are not independent. This is particularly evident for the $\text{H}\alpha$ line (Figure 6), where the very broad component (presumably from the nucleus) can still be seen at $1.4''$ to $2''$ from the nucleus. Nevertheless, by isolating the narrow line component, we should be isolating the emission from the low-density

gas.

The only position angles covering this redshifted velocity peak which were observed in *both* the red and the blue spectral region are those in PA 102° and 128° . The line ratios from these spectra (uncorrected for reddening) for the emission lines $[\text{OIII}] (5007)/(\text{H}\beta)$, $([\text{SII}] 6716+6731)/(\text{H}\alpha)$, $([\text{NII}] 6583)/(\text{H}\alpha)$, and $([\text{OI}] 6300)/(\text{H}\alpha)$ are shown in table 3. We have observed stellar flux calibration standards for all of these spectra and have used them to estimate the *relative* corrections to the ratios in table 3. Even in the most extreme cases ($[\text{O I}] : \text{H}\alpha$) these are less than ± 0.04 in the log (much less than the errors from “noise” for the emission at distances greater than $0.2''$ from the nucleus - which are ± 0.15 in the log). We reiterate here the important observational point made by Veilleux and Osterbrock 1987: *Absolute* flux measurements are very difficult to accomplish, while diagnostic *line ratios* for adjacent emission lines taken simultaneously can be very accurate. The correction for differential atmospheric refraction between $[\text{O III}]-\lambda 5007$ and $[\text{O II}]-\lambda 3727$ is well known to be in excess of $0.3''$ even for “reasonable” zenith angles and even for one spectrum with the exposure times reported here. When transferred *between* objects (standard star to galaxy) this can easily amount to a 30% error (under ideal conditions with an ideal spectrograph).

2. *The N Optical–Radio “Pseudo–Ring”:* The most mysterious feature seen in the optical–radio images is the large arc or loop to the NW (at $\sim 4''$ in PA $\sim 255^\circ$), where the a bubble in the ATCA, 3 cm image crosses the $\text{H}\alpha$ pseudo–ring (Figure 1b inset.) We have no spectra which cover this position angle directly. The closest coverage is along the spectrum in PA 0° . For completeness, we have also measured line ratios for this spectrum. These are included in table 3.
3. *Diagnostic Diagrams:* The line ratios are plotted in Figure 7 (a–c) as diagnostic “BPT” diagrams (Baldwin et al. 1981, Veilleux and Osterbrock 1987). The solid curve in each case represents the division between HII region like objects and narrow emission–line galaxies such as Seyfert 2, NLRG, and “liners” (as indicated by the empirical delineations in Veilleux and Osterbrock 1987.) The $([\text{NII}] 6583)/(\text{H}\alpha)$ measure-

ments appear to be inconsistent with the [OI] and [SII] measurements. The latter clearly lie to the right of the curve delineating the HII region-galaxy separation while the [NII] measurements lie to the left of the corresponding curve in the [OIII] (5007)/(H β)—([NII] 6583)/(H α) plane. The reality of this effect can be seen in the line plots shown in Figure 6, where the nuclear spectrum in the region of H α –[NII] from PA 102 $^\circ$ is shown plotted to the same scale as the corresponding spectra at 0.73, 1.46, and 2.25'' W of the nucleus. (The relative scaling amounts to roughly a factor 8 between the nuclear spectrum and that at 2.25'' W.) The redshift (seen as the redshifted velocity plume in Figure 5b) clearly shows up in the narrow line region of both the H α and the [NII] lines. The single large circle and square plotted in each diagram refer to values of line ratios from a model by Ferguson et al. 1997 and will be discussed in section 4.

4. *[SII] Line Ratios:* Finally, we determined the [SII] (6717/6731) ratios for the regions in question (table 4), as a check on our assumption that the measured lines come from the low-density region outside the nucleus. These do show a slight tendency to decrease with distance from the nucleus (corresponding to a density change in N_e from roughly 10^3 to 10^2 (with $T = 10,000$ $^\circ$ K) (Osterbrock 1989). We note, however, that although the *trends* seen in the densities inferred from these [SII] emission lines are probably real, the *densities* probably cannot be derived directly from the measured line ratios (cf. Ferguson et al. 1997.)

3. HST Observations

The primary goal of our HST observations was to measure the size of the narrow-emission-line region (NLR) surrounding the nucleus, and to search for morphological features (such as a compact, double nucleus, or an optical jet related to the radio emission) which might provide clues about the mechanisms feeding the nuclear energy source. Current physical models predicted that the nucleus of this object should be a point source and contain roughly 90% of the total flux observed from the ground within 1''. Our CTIO spectral measurements (above) yield a lower limit to the total flux in the [O III] λ 5007/4958 lines of $10^{41}h^{-2}$ erg s $^{-1}$. Using this and standard

parameters for the emitting gas clouds, we estimated the scale of the transition region between narrow-line and broad-line emission to be 75–150 pc (or $\sim 0.15''h$ to $\sim 0.30''h$, roughly 3.5 to 7 pixels at 43 mas pixel $^{-1}$ the scale of the original HST Planetary Camera.

3.1. The Choice of Camera and the Under-sampling Problem

We chose to observe Pictor A with the Planetary Camera (PC) (Westphal et al. 1982) because the ability of the CCD detector to accept high photon count rates would minimize observing time and maximize signal to noise in the fainter, diffuse regions adjacent to the nucleus. In addition, the filters available on the original WF/PC included one which would isolate the redshifted [OIII] emission (F517N) and this presented an excellent opportunity to image one of the more important NLR components for this powerful, nearby FR II radio galaxy. When it became clear that the original HST camera/mirror suffered from spherical aberration we decided to go ahead with a subset of the proposed observations on Pictor A because we believed (correctly, it turned out) that any subsequent repair would eliminate the F517N filter and thus rule out the possibility of imaging the [OIII] region. With the aberrated images found in Cycle 1 and Cycle 2 data, it was necessary to increase the observing time by a factor of 7 over unaberrated exposures to compensate for the increased photon noise from the scattered light in the diffuse regions surrounding the nucleus.

3.2. The HST Data

During Cycle 1, Pictor A was observed through the F517N and F547M filters on Sept. 12, 14, 15, and Oct. 8, 1991 (table 3). The F517N filter was centered on the $\lambda\lambda$ 4958 and 5007 emission lines from [OIII] while the F547M filter includes these emission lines at its blue end, with roughly the same transmission, but also transmits approximately five times more continuum emission than the F517N filter (WFPC Handbook, 1989). Our objective was to separate out the NLR from the continuum emission by subtracting the different filter images.

During Cycle 2, Pictor A was observed through the F648M and F718M (WFPC Handbook, 1989) filters on Sept. 20, 1992 (table 3). The F718M filter covers the emission lines from H α , λ 6563, [NII] $\lambda\lambda$ 6527, 6548, 6583 and [SII] $\lambda\lambda$ 6717–6731, while the F648M

filter includes both the [OI] emission lines at $\lambda\lambda$ 6300, 6363 which appear in the ground-based nuclear spectrum at a factor of ~ 20 less intensity than the $H\alpha$ emission line (cf. the inset in Figure 6). The F648M filter also includes the $H\alpha$ and [NII] lines, but at a reduced transmission of roughly a factor of 2.5. Our objective here was to separate out the $H\alpha +$ [NII] emission line regions from the continuum emission, although the filter combination was far less favorable for this than the one isolating [OIII] in Cycle 1.

The exposure times for these observations were calculated from the published transmission-detector curves for the HST PC (WFPC Handbook, 1989) and our nuclear spectra for Pictor A (described above). The difficulties for this type of calculation are twofold: 1) The filter transmissions change with time and temperature, and transmission values for wavelengths near the filter edge (such as the [NII], $H\alpha$ group in the F648M filter) may vary significantly, and 2) The nuclear emission line spectrum of Pictor A is known to vary (Filippenko 1985, Sulentic et al. 1995, Halpern et al. 1996) and the change in flux can (and evidently did - see section 3.3.3) lead to saturated images.

Both the Cycle 1 and the Cycle 2 observations had the obvious drawback that the true, observed PSF for this object would have an “effective filter” which was a function of the relative emission-line strengths at each point and their redshifted wavelength. However, this is a secondary effect compared with the aberration problem.

3.3. HST Data Analysis

All of the observations were normalized and bias corrected using the most proximate calibration frames in the data base. They were cleaned of cosmic ray “hits” using standard STSDAS WFPC analysis routines.

Since the HST primary mirror has a diffraction-limited resolution of 57.7 mas at 550 nm and 37.8 mas at 720 nm, the PC data, with a grid size of 0.042 mas pixel⁻¹ is not properly sampled. Thus, to construct a properly sampled image for our Cycle 1 data we chose to “dither”, i.e., observe the object at four slightly shifted positions (offset in Δx and Δy by different pointing combinations of 0.022 mas as shown in Figure 8a.)

In fact, because of scheduling constraints, this dither scheme was not used and the observations for Cycle 1 were offset by random pixel shifts, at different space-

craft roll angles. The offsets were measured using two methods; 1) crosscorrelation of individual images taken through the same filter (using the 14/09/91 data as a reference) and 2) using the “imcnt” routine in IRAF to measure the pixel coordinates of the bright, nuclear region. These methods gave results which agreed to within less than 0.05 pixel. The measured pixel shifts are given in table 3 (and shown graphically in Figure 8b). In addition, there was a systematic shift between the images taken through the F517N filter and the F547M filter. This amounted to -0.90 ± 0.06 in x and $+0.10 \pm 0.05$ in y (in good agreement with independently measured values of -0.69 and -0.05 by Evans 1991. The F517N images were shifted by this additional amount after deconvolution.

3.3.1. Analysis of Composite Images

Many different schemes have been developed for “dithering” image data before “cleaning” restoring it with a more visually interpretable PSF. Several of these and their applicability to HST Cycle 1 and Cycle 2 data are described in Hanish and White 1994. Because our Cycle 1 data is unique, we outline the scheme we used here:

A rotated image is the same as a non-rotated image convolved with a PSF of opposite rotation. That is, if I_i is an image at roll angle i and e_i is its exposure time, then:

$$(I_1 * P)_{\theta} + (I_2 * P)_{\theta} + (I_3 * P)_{\theta} + (I_4 * P)_{\theta} = I_{\theta} * \left(\sum P_{-i} \cdot e_i \right) \quad (1)$$

where I_{θ} and P are the image and PSF at θ° , the subscript θ outside the parentheses means the image has been rotated back to θ° , and P_{-i} is the PSF at θ° rotated through the negative roll angle, $-i$. Thus,

$$P_T \equiv \left(\sum P_{-i} \cdot e_i \right) \quad (2)$$

becomes a new, composite PSF for the composite image which is the sum of the individual images shifted to a common center and rotated back to a common position angle, θ .

Note that since the rotation operation can be expressed in terms of two orthogonal functions (sine and cosine), as long as two conditions hold: a) the under-sampling is less than a factor of 2, and b) for each frame, if Δp is the pixel size, and both the offsets

from the common center, Δx and Δy , include a pixel fraction, f_p , such that

$$0.25\Delta p \leq f_p \leq 0.5\Delta p, \quad (3)$$

then all of the pixels in the registered images will have sufficient offset spacings to sample a different part of the image. Both these conditions hold for the Cycle 1 data discussed here.

One advantage of this serendipitously employed technique is that the composite PSF, P_T , is much more radially symmetric, with the “tendrils” de-emphasized (and thus, their propensity to induce artificial, radially extensive features minimized).

4. The Restored HST Images

4.0.2. Cycle 1 Results

The technique described above was applied to our Cycle 1 data which was resampled on a double grid, shifted to a common center, rotated using a sinc interpolation, and then co-added. One set of PSF’s used for deconvolution was generated in the same way starting with a set of *observed* PC6 PSFs at 502nm (supplied by Ed Groth and Jim Westfall, and regridded to reflect the slight change in the PSF between 502nm and 517nm). These were slightly shifted from the PC6 position of the galaxy nucleus but, again, this (along with the slight mis-match in effective wavelength of the PSFs) is a secondary effect. A second set of PSFs was generated using the “Tiny Tim” optical modeling software (Burrows et al. 1991; Krist 1994). The relevant central parts of these two PSFs are shown in Figure 9a and b. Their ratios (observed / calculated) are shown in Figure 9c. The principal difference between the two PSFs is the fine detail in the area around the central pixel which is found in the “Tim” PSF and not in the “observed” one. This amounts to a 10% amplitude difference and appears to influence the final deconvolution result (see section 3.3.2.)

The composite images were restored using both of these different sets of point-spread functions and a Maximum Entropy algorithm, with a front end (MEM) developed by Weir (1991a; 1991b). Since the strong [OIII] emission lines from the nuclear region of Pictor A are included in both the F517N and F547M band passes, the PSF structure will be determined primarily by these narrow emission lines, which are better approximated by the F517N PSF. Thus the

approximate F517N PSFs were used for deconvolving both the observations through the F547M filter and those through the F517N filter.

The discussion above makes it clear that we do not have a perfect, mathematically correct, set of data for deconvolution analysis. Nevertheless, we have taken an experimental approach, doing scores of deconvolution calculations, using different combinations of what seem to be “reasonable” approximations to the PSFs, image subtraction procedures, and deconvolution criteria. All of these different calculations produce images which share the same general features.

The two most extreme results for the two filter sets (F517N and F547M) are presented here. These two extreme cases differ in deconvolution procedures in two important ways: 1) one set (shown in Figure 10 a and c and 11 a, b, and c) uses the “observed” PSFs while the other (Figure 10 b and c and 11 d) uses the “Tim” PSFs and 2) the registration and construction of the raw images and PSFs for the images in Figure 10 a and c and 11 a, b, and c was done in such a way that North was towards the left (decreasing x) side of the frame while the images shown figures 10 b and d and 11 d were oriented with North pointing at -21.72° (i.e. clockwise) from the increasing y axis. (All images have been rotated to the normal astronomical coordinate system in figures 10 and 11.) These different orientations were chosen to examine the influence of the coordinate grid orientation on the final deconvolution result. It proved to be as important as the difference in PSF images.

The results for the F547M images are shown in Figure 10a-d. Both reconstructions give approximately the same normalized peak flux for the nucleus (11,800 using the “observed” PSF with results shown in Figure 10 a and 13,500 using the Tiny Tim PSF, with results shown in Figure 10 b). The images in Figure 10 c and d have been corrected for the [OIII] emission by subtracting off 54% of the flux in the F517N images (the 54% contribution was calculated using the filter/instrument response curves in the WFPC Handbook, 1989. These values clearly are not stable, but are probably no more in error than any of the other assumptions and approximations used in this analysis. The Tiny Tim PSF yields images which are consistently more “point like” than those deconvolved with the observed PSF. This seems to be related to the difference in PSF structure shown in Figure 9 c. We conjecture that the fine detail in the off-center structure of the Tim PSF leads the deconvolution algorithms

to treat the measured photons in extended, smooth structures as “noise”, forcing them into any adjacent point sources. Both reconstructions show what appears to be real structure outside the nucleus.

In particular, there is evidence for a small continuum feature in the direction of the large-scale radio structure (shown as arrows in Figure 10 c and d, corresponding to the arrows shown in Figure 2 inset) with a peak flux which is $\sim 4\%$ of that in the unresolved nucleus in Figure 10 a and $\sim 3\%$ in 10 c with corresponding values of $\sim 3\%$ and $\sim 2\%$ for the images in figures 10 b and d, respectively. This feature consistently showed up in all of our F547M reconstructions with peak intensity values ranging from 22:1 to 55:1 relative to the nucleus. This feature is certainly continuum emission, not emission from ionized gas. (It does not show up in the [OIII] image, Figure 11.) It could be a faint star or scattered light from the nucleus but the probability of such an accidental alignment with both the outer radio structure and the VLBI jet (see section 3.5, below) is quite low. The most likely possibility is that it is associated with the radio structure in Pictor A.

The deconvolutions for the F517M images using the “observed” PSF are shown in Figure 11 a and b. Figure 11 a shows a gray-scale plot of the deconvolved F517N image (uncorrected for continuum). Isophototes for the deconvolved F547M image (obtained with the same PSF) are superimposed. Figure 11 b shows the deconvolved F517N image plotted alone. Note the broad plateau to the N of the nuclear peak. Figure 11 c is the deconvolved F517N image (observed PSF) corrected for continuum by subtracting off 30% of the deconvolved F547M image (again, the relative [OIII] – continuum contributions to the two filters are based on the data from the WFPC Handbook, 1989). Finally, Figure 11 d shows the result of deconvolving the *difference* between the two observed images with the “Tiny Tim” PSF (i.e. subtracting 30% of the F547M image from the F517N image with the grid oriented as it was for the images in figures 11 b and d and then doing the deconvolution). The most notable features in these images are: 1) In both (very different) deconvolution results the [OIII] emission is extended by ~ 150 mas to the NW, *outside* of the path of the “jet” or “bridge” (again shown by the arrows.) 2) In both images (Figure 11 c and d) the [OIII] emission peaks at a point located ~ 60 mas to the *NE* of the nuclear position.

4.0.3. Cycle 2 Results

We obtained two further sets of images with the HST PC in Cycle 2, using medium-width filters centered at 648 nm (F648M) and 718 nm (F718M). As noted above in section 3.2), the F718M filter covers the emission lines from $H\alpha$, λ 6563, [NII] $\lambda\lambda$ 6527, 6548, 6583 and [SII] $\lambda\lambda$ 6717, 6731, while the F648M filter includes both the [OI] emission lines at $\lambda\lambda$ 6300, 6363.

The Cycle 2 exposures, were scheduled and taken before the Cycle 1 data had been analyzed, and were designed to obtain maximum signal-to-noise, without “dithering” in the allotted spacecraft time. The images were all recorded on the same place on the PC 6 chip (to within 0.05 pixel) and with the same roll angle. Thus the images could not be shifted and treated as a fully sampled image set, making it impossible to recover the full resolution of the telescope as was done with the Cycle 1 images. In addition, the F718M images were saturated in the nucleus, suggesting that this filter contained more of the broad nuclear $H\alpha$ emission line than we had calculated (probably because the flux in the $H\alpha$ line had increased since our CTIO observations, Filippenko 1985, Sulentic et al. 1995, Halpern et al. 1996.)

Nevertheless, these Cycle 2 images were also double binned and co-added. The image in Figure 12a is an attempt to smooth the F648M image to a resolution of $\sim 1''$ for comparison with our ground-based $H\alpha$ image. However, there are not sufficient detected photons in the F648M frames to provide a reliable, low-resolution image. The Weir “MEM” restorations were done for the two filter data sets using “Tiny Tim”, composite PSFs at the correct wavelength. The results for the F648M filter are shown in Figure 12b. (The results for the F718M images are not worth publishing.) It is clear that this reconstruction displays no extended structure beyond that expected from the distortion of the aberrated PSF itself, and no attempt was made to do the type of filter subtraction which was successful for the Cy 1 data. The most logical explanation for this “failure” is simply the fact that the data for Cycle 2 are undersampled (and saturated for the F718M filter data).

4.1. Comparison of the HST Images with a VLBI Core Jet

After our initial reductions of our Cycle 1 HST data (in June of 1992), when we had identified the

continuum knot or “jet” seen in Figure 10a (and before Perley et al. 1997 had firmly concluded that there was a “bridge” linking the NW hotspot to the core in their 20 cm data), we learned that the 2.291 GHz data from the SHEVE VLBI array (Tingay et al. 1999), taken roughly half a year before our HST Cycle 1 data, showed evidence for an extended structure in the “E-W” direction. Subsequently, two additional sets of SHEVE data, at 8.4 GHz, were obtained (in February and July, 1993, Tingay et al. 1999.)

Two of the SHEVE images (2.291 and 8.418 GHz) are over plotted on one of our HST F547M restorations Figure 13.m (The 2.291 GHz data defines the outer contours of the inset image and the 8.418 data is shown as gray-scale.) The HST “continuum” image plotted in Figure 13 has been corrected for [OIII] emission (as described in section 3.4.1). It differs from the restorations shown in figures 10 and 11 in the way the gridding was done before deconvolution. The HST image in Figure 13 was restored with a “Tim” PSF (see section 3.3.2) but the prerestoration grid was oriented in the normal (E to left N to top) astronomical system. The “boxy” nature of the central isophotes which seem to be associated with this grid orientation can be seen in Figure 13.

Although the SHEVE images have too low a dynamic range to identify any direct correlation between the HST continuum image knot and the radio structures (Tingay et al. 1999), the alignment is certainly suggestive (as is the overall relationship between the VLBI jet, the HST continuum, and the HST [OIII] image morphology – see section 4 below.)

5. Discussion

This compendium of data marks the first time that both optical and radio measurements have been available at such high spatial resolution for a well-defined FR II radio galaxy. Although there is a wealth of details in the data, our objective in this paper is to focus on the features in the different data sets which enhance our understanding of the relationship between the beamed radio plasma and the ambient interstellar medium in such galaxies. The following points appear significant:

5.1. Relationship Between the Small-scale and Large-scale Morphology

Within the resolution of our HST images, the spatial relationship between the radio and optical fea-

tures on different scales appears to be homologous.

The most obvious morphological similarities are those involving alignment. The VLBI jet, the HST continuum feature, the end of the H α “bridge” in PA 283°, the 20 cm VLA “bridge”, and the direction between the nucleus and the outer hot-spots all lie within the range PA 280° – 288 °.

A more subtle morphological similarity seems to occur in the offsets between the continuum and emission features. On the pc–mas scale, the optical *continuum* feature and VLBI jet are nearly aligned but the [OIII] line emitting region is extended (by roughly 200 mas or 110 pc h⁻¹) to the NW (Figure 11 b and d.). On the kpc scale, the VLA bridge and the direction to the NW hot-spot are aligned but the H α bridge, which extends to the NW, lies slightly to the N of a line linking the nucleus with the jet–hot-spot direction. In both cases, on very different scales, the line emitting gas appears to the N of the channel defined by the radio beam.

There is also an asymmetry in the central brightness of this object which shows up on both the 100 pc and the kpc scales. Referring back to Figure 5a, the steepness of the continuum intensity gradient on the S side of the galaxy also shows up in the H α image (Figure 5b), where the nucleus of the galaxy (at 0,0 in the plot) lies to the S of the brightest H α emission. Turning to the plots in figures 11c and d, we see that there the brightest [OIII] emission also lies to the N (and slightly E) of the nucleus. This asymmetry *may* be caused by dust in the nucleus (cf. Knapp et al. 1990 for a discussion of the IRAS data) but, again, it may be associated with the asymmetry in the velocity field and the 3 cm ATCA feature seen to the N of the nucleus (below).

Finally, and most puzzling, the Kpc scale “pseudo-ring” and 3 cm feature seen to the N of the optical nucleus seem to have a small-scale counterpart in the peri-nuclear [OIII] emission found with the HST. Although the resolution of the latter image is marginal, it appears as a ring-like feature with an enhanced brightness to the N in figure 11 c and as an extended envelope with a point-like enhancement to the N in figure 11 d. In this case, the emitting gas seems to take on a ring-like structure at very different scales.

The overall impression which one receives from these morphological homologies is that the radio jet or beam is pushing the ambient interstellar gas to the N in its passage out from the nucleus.

5.2. Orientation of the Velocity Structure in the EELG

Two characteristics of the velocities seen in figures 4 a–h and 5 b imply a correlation between the kinematic features of the EELG and the beamed radio plasma:

1. The initial impetus for our CTIO spectroscopy program was to obtain sufficient information about the velocity field in the EELG to separate out large-scale rotational motions (if any) from more chaotic flows in the gas. Although we do not have complete coverage of the galaxy, there does appear to be a “null” in the overall large-scale velocity field at \sim PA 285° –PA 295° . This is consistent with the picture that well-defined FR II radio galaxies have radio axes which are correlated with the projected rotation axes of their gas (Simkin 1979, Heckman et al. 1985.)
2. Of more direct relevance to the question of interaction between the radio plasma and the ambient interstellar gas is the red-shifted velocity “plume” seen in the direction of the jet–bridge–radio lobe alignment (Figure 5b.) Although the relative projected velocities are small (the maximum deviation from “circular velocity” in Figure 4f seems to be $\sim 60 \text{ km s}^{-1}$), this lends strong support to the morphological evidence that the radio plasma has “clobbered” the interstellar gas. There is, however, the alternative possibility that the counter velocities seen on the W side of the nucleus are not the result of disturbance by the radio plasma but are, instead, a gravitationally induced flow in response to a non-axisymmetric potential. This latter type of velocity disturbance would most likely have a signature which showed up as a counter flow in \sim PA 30° – 90° where our spectral coverage is poor. Thus it cannot be completely ruled out.

5.3. Emission Line Ratios

The most outstanding feature of the emission line ratios in table 3 and Figure 7 is the very low value of $[\text{NII}]:\text{H}\alpha$. Although the $[\text{SII}]:\text{H}\alpha$ and $[\text{OI}]:\text{H}\alpha$ plots (Figure 7a and b) appear to place these regions in the upper envelope of the “AGN region” (shown in Veilleux and Osterbrock 1987), the $[\text{NII}]:\text{H}\alpha$ ratios (Figure 7c) lie in the area of the diagram occupied

by H II regions. The AGN spectra which appear to bear the most similarity to the spectrum of Pictor A in Figure 6 are those of Seyfert 1.5 and 1.8 galaxies. However, the latter objects do not have the relatively high ratios of $[\text{OI}]:\text{H}\alpha$ and low ratios of $[\text{NII}]:\text{H}\alpha$ seen here (Cohen 1983).

There are reports in the literature of EELG with low $[\text{NII}]:\text{H}\alpha$. Most commonly, these seem to gas clouds which are clearly associated with or entrained in a radio jet. The data for these objects has been summarized by Viegas and de Gouveia Dal Pino 1992. More recently, the EELG associated with the hot-spot and SE radio lobe in PKS 1932-464 studied by Villar-Martin et al. 1998 and for PKS2250-41 by Clark et al. 1997 have also been observed. In all of these cases, however, although the reported values for $[\text{NII}]:\text{H}\alpha$ and $[\text{OI}]:\text{H}\alpha$ are lower than those usually found for active galaxy nuclei, none of the examples are as extreme as the ones we have found for Pictor A (including its nuclear values).

As noted earlier, there are competing models for calculating the expected emission line ratios from shock heating and/or UV continuum excitation and ionization for the EELR in galaxies as well as the nuclear spectrum of AGNs. Baum and Heckman 1989b give a good summary of the field up to that date. More recently, additional, more complex calculations have been carried out (Viegas and de Gouveia Dal Pino 1992, Dopita and Southerland 1995, Storchi-Bergmann et al. 1996), Ferguson et al. 1997, Allen et al. 1998 and references therein.)

Although all of these models do manage to fit the observed line ratios found in H II regions and AGN spectra, none of them, with the exception of models recently published by Ferguson et al. 1997, reproduce the extreme values of the $[\text{OI}]$ and $[\text{NII}]$ ratios reported here. The predicted line ratios from Ferguson et al. 1997 which do seem to fit our present values are plotted as large open circles and squares for the diagnostic planes in Figure 7. These correspond to models in which the covering factor for clouds drops off much more slowly with radial distance from the ionizing source than is the case for models which fit the observed spectra of most AGNs (“Dusty” models where the cloud covering fraction falls off roughly as $r^{-1.25}$ and $n^{-1.0}$ and “solar abundance” models where it falls off as $r^{-0.75}$ and $n^{-1.0}$, Ferguson et al. 1997).

However, it is difficult to reconcile the reasonably good fits to some of the Ferguson et al. 1997 spectral models with the geometry of the EELG which we

observe in Pictor A. Although the gas in the regions $2''$ – $3''$ (1 to $1.6 \text{ kpc} h^{-1}$) may well receive ionizing radiation from the nucleus, the fact that strong [OI] emission is found only in the non–nuclear region associated with the velocity “plume” and the direction of the $H\alpha$ and VLA bridge suggests that there must also be some energy input to the gas from either shocks or cosmic rays associated with the radio plasma.

6. Conclusions

By combining a series of high angular resolution observations at multiple frequencies, we have been able to establish a fairly convincing case for the direct physical disruption of the interstellar medium in the inner regions of a classical FR II radio galaxy. In particular, we find morphological features which suggest that the structural disruption extends over scales ranging from a few hundred parsecs to several kpc. One of the spectral signatures of this disrupted gas appears to be anomalously weak line strengths for [NII] compared with $H\alpha$. Although the low emissivity from the [NII] line may reflect intrinsically low N abundances in this particular radio galaxy, it seems likely that it may be related to the excitation mechanism for these gas clouds.

All observational papers end by concluding that more and better data are needed to answer the questions raised by the data reported. In this paper we wish to vary that theme somewhat. What is needed, if we are to achieve a better understanding of the physics of radio jets and their ambient medium is not *more* data but *different* data. In particular, we emphasize the importance of obtaining high resolution measurements (both spatially and spectroscopically) of the entire velocity field in the EELG of nearby radio galaxies. Only by obtaining very high angular resolution measurements for the very closest objects will we have sufficient spatial resolution to permit sensible comparison with spectral models.

This work is based on observations with the NASA/ESA Hubble Space Telescope obtained at the Space Telescope Science Institute, which is operated by Association of Universities for Research in Astronomy, Incorporated, under NASA contract NAS5-26555 and with financial support from HST grant GO-245601-87A. We thank both CTIO (operated by AURA under contract to the US NSF) and the ATNF (funded by the Commonwealth of Australia for operation as

a National Facility managed by CSIRO) for observing time and support. Part of this work was done with financial support from NSF (AST-8914567) partial publication costs came from a grant (to SMS) from NASA, administered by the American Astronomical Society). The graphics in this paper were generated with the software package *WIP*⁶, using the *PGPLOT*⁷ graphics library. This research has made use of the NASA/IPAC extragalactic database (ned) which is operated by the Jet Propulsion Laboratory, Caltech, under contract with the National Aeronautics and Space Administration. We thank Ed Growth and John Mackenty for help obtaining observed PC PSFs, John Kriss for producing the “Tiny Tim” software, and Ian Evans for help with N. Weir’s memsys routines.

REFERENCES

- Allen, M., G., Dopita, M., A., Tsvetanov, Z., I., and Southerland, R., S., 1998, *ApJ*, 493, 571
- Australia Telescope 1992, *J. Electr. Electron. Eng. Aust.*, Special Issue, 12, No. 2, editors, R.H. Frater and J.W. Brooks
- Baldwin, J.A., Phillips, M.M., and Terlevich, R., 1981, *PASP*, 93, 5
- Baum, S. A., Heckman, T. M., Bridle, A., Van Breugel, W., Miley, G. K., 1988, *ApJS*, 68, 643
- Baum, S. A., and Heckman, T., 1989, *ApJ*, 336, 681
- Baum, S. A., and Heckman, T., 1989, *ApJ*, 336, 702
- Burrows C. J. et al. 1991, *ApJ*, 369, L21
- Carswell, R.F., Baldwin, J. A., Atwood, B. and Phillips, M. M., 1984, *ApJ* 286, 464
- Christiansen, W.N., et al., 1977, *MNRAS*, 181, 183
- Clark et al., 1997, *MNRAS*, 286, 558
- Cohen, R. D., 1983, *ApJ*, 273, 489.
- Conway J.E., Cornwell T.J., Wilkinson P.N., 1990, *MNRAS*, 246, 490
- Dopita, M., A., and Southerland, R., S., 1995, *ApJ*, 455, 468

⁶*WIP* is copyright by the Berkeley-Illinois-Maryland Association (BIMA) Project Morgan 1995

⁷software copyrighted by California Institute of Technology

- Evans, Ian, private communication.
- Ferguson, J., W., Korista K., T., Baldwin J., A., and Ferland G., J. 1997, *ApJ*, 287, 122
- Filippenko, A., 1985, *ApJ*, 289, 475
- Fraix-Burnet, D., Golombek, D., Macchetto, F., Nieto, J., Lelievre, G., Perryman, M. A. C., Di Serego Alighieri, S. 1991, *AJ*, 101, 88.
- Grimberg, B. I., Simkin, S. M., and Sadler, E. M., 1999, *ApJ*, submitted (MS#39792)
- Halpern, J. P., Eracleous, M., Filippenko, A. V., Chen, K. , 1996 *ApJ*, 464, 704
- Hanish, R.J., and White.R.L., "The Restoration of HST Images and Spectra," 1994, Space Science Telescope Institute, Baltimore, MD
- Hansen, L., Jorgensen, H. E., Norgaard-Nielsen, H. U., 1987, *A&AS*, 71, 465
- Heckman, T. M., Illingworth, G. D., Miley, G. K., Van Breugel, W. J. M. *ApJ*, 1985, 299, 41
- Jenkner, H., Lasker, B. M., Sturch, C.R., McLean, B.J., Shara, M. M. and Russell, J. L., 1990, *AJ*, 99, 2081
- Knapp, G. R., Bies, W. E., Van Gorkom, J. H., *AJ*, 1990, 99, 476
- Krist, J. E., HST Tiny Tim Software, Version 4.0b release September 1994
- Lasker, B. M., Sturch, C. S., McLean, B. J., Russell, J. L., Jenkner, H., and Shara, M. M. 1990, *AJ*, 99, 1019
- MacKenty , J.W., Simkin, S.M., Griffith, R.E., Ulvestad, J.S., and Wilson, A.S. 1994, *ApJ*, 435, 71
- Morgan, J. A. 1995, in "Astronomical Data Analysis Software and Systems IV", *PASP Conf Series* 77, editors R. A. Shaw, H. E. Payne, and J. J. E. Hayes, p. 129.
- Osterbrock D., "Astrophysics of Gaseous Nebulae and Active Galactic Nuclei, 1989, page 134, University Science Books, Mill Valley, CA.
- Perley,R.A., Röser, H.-J., and Meisenheimer, K. 1997, *A&A*, 328, 12
- Prieto, M. A., Walsh, J. R., Fosbury, R. A. E., Di Serego Alighieri, S. 1993, *MNRAS*, 263, 10
- Reynolds J.E., 1994, *ATNF Technical Document Series* 39.3/040
- Röser, H.-J., and Meisenheimer, K. 1997, *ApJ*, 314, 70
- Robinson, A., Binette, L., Fosbury, R. A.,E., and Tadhunter, C. N., 1987, *MNRAS*, 227, 97
- Russell, J.L., Lasker, B. L., McLean, B. J., Sturch, C. R., and Jenkner, H., 1990, *AJ*, 99, 2059
- Sault R.J., Wieringa M.H., 1994, *A&AS*, 108, 585
- Sault R.J., Teuben P.J, Wright M.C.H, 1995, eds. R. Shaw, H.E. Payne, J.J.E. Hayes, *Astronomical Data Analysis Software and Systems IV*, A.S.P., 77, 433
- Simkin, S.M., , 1979, *ApJ*, 234, 56
- Storchi-Bergmann, T., Wilson, A., S., Mulchaey, J., S., and Binette, L., 1996, *A&A*, 312, 357
- Su, H-J., and Simkin, S. M., 1980, *ApJ*, 238, L1
- Sulentic, J. W., Marziani, P., Zwitter, T., Calvani, M. 1995, *ApJ*, 438, L1
- Tadhunter, C. N., Fosbury, R. A. E., and Quinn, P. J., 1989, *MNRAS*, 240, 225
- Thomson, R. C., Crane, P., and Mackay, C.D., 1995, *ApJ*, 446, L93
- Tingay, S.J., et al., 1999, submitted to the *ApJ*
- Veilleux, S., and Osterbrock, D., *A&AS*, 1987, 63, 295
- Viegas,S.M. de Gouveia Dal Pino,E.M., 1992, *ApJ*, 384, 467
- Villar-Martin, M., et al. 1998, *A&A*, 332, 479
- Weir, N. 1991a, *ESO Workshop No. 38*, P. J. Grosbol and R. H. Warmels, *ESO*: 115
- Weir, N. 1991b, 10th International Workshop on Maximum Entropy and Bayesian Methods, editors W. T. Grandy and L. H. Schick, (Dordrecht: Kluwer), 275
- Westphal et al. 1982, *The Space Telescope Observatory*, D. N. B. Hall, *NASA*: CP-2244, 28

Hubble Space Telescope Wide Field and Planetary
Camera Instrument handbook, version 2.0, May,
1989

Wilson A. S. and Baldwin J. A. 1985, ApJ, 289, 124

TABLE 1
CTIO - 1.5M - OPTICAL IMAGES

DATE	AIRMASS	FILTER	EXP TIME	SEEING (FWHM)
27/28 Feb 1987	1.09	6826/78 line	2000 s	1.7''
27/28 Feb 1987	1.14	6560/110 cont	2000 s	1.7''
27/28 Feb 1987	1.22	6826/78 line	2000 s	1.7''
28 Feb/1 Mar 1987	1.46	6826/78 line	2000 s	1.5''
28 Feb/1 Mar 1987	1.69	6560/110 cont	2000 s	1.5''

TABLE 2
CTIO - 4M - SPECTRA

DATE	SLIT PA	WAVELENGTH RANGE
19/20 Feb 1987	90°	6473 - 7163 Å
19/20 Feb 1987	12°	6473 - 7163 Å
19/20 Feb 1987	0°	6473 - 7163 Å
20/21 Feb 1987	102°	6473 - 7163 Å
20/21 Feb 1987	115°	6473 - 7163 Å
21/22 Feb 1987	128°	6473 - 7163 Å
21/22 Feb 1987	50°	6473 - 7163 Å
22/23 Feb 1987	102°	4882 - 5729 Å
22/23 Feb 1987	128°	4882 - 5729 Å
14/15 Jan 1988	30°	6653 - 7338 Å
15/16 Jan 1988	30°	4895 - 5746 Å

TABLE 3
EMISSION LINE RATIOS

PA($^{\circ}$)	dist from Nuc ($''$)	$\log([\text{O I}]/\text{H}\alpha)$	$\log([\text{N II}]/\text{H}\alpha)$	$\log([\text{S II}]/\text{H}\alpha)$	$\log([\text{O III}]/\text{H}\alpha)$
0	0.00	-0.240	-0.651	-0.132	...
90	0.00	-0.454	-0.748	-0.344	...
102	0.00	-0.466	-0.775	-0.231	0.461
115	0.00	-0.518	-0.726	-0.242	...
128	0.00	-0.563	-0.706	-0.334	0.464
0	0.73 N	-0.410	-0.615	-0.022	...
0	0.73 S	-0.354	-0.654	-0.211	...
90	0.73 W	-0.550	-0.806	-0.155	...
102	0.73 W	-0.561	-0.759	-0.266	0.558
115	0.73 W	-0.561	-0.759	-0.266	...
128	0.73 W	-0.521	-0.743	-0.259	0.512
0	1.45 N	-0.610	-0.559	0.050	...
0	1.45 S	-0.575	-0.744	-0.370	...
90	1.45 W	-0.614	-0.853	-0.114	...
102	1.45 W	-0.320	-0.699	-0.175	0.516
115	1.45 W	-0.504	-0.819	-0.465	...
128	1.45 W	-0.528	-0.689	0.013	0.476
0	2.20 N	-0.579	-0.551	0.025	...
0	2.20 S	-0.470	-0.547	-0.225	...
90	2.20 W	-0.640	-0.727	-0.048	...
102	2.20 W	-0.182	-0.588	-0.114	0.451
115	2.20 W	-0.465	-0.728	-0.503	...
128	2.20 W	-0.489	-0.748	-0.111	0.547
0	3.00 S	-0.636	-0.512	-0.214	...

TABLE 4
[SII](6717/6734)

PA	Nucleus	0.73" W	1.46" W	2.25" W	3.00" W
(error)	(0.06)	(0.06)	(0.06)	(0.15)	(0.30)
90.0	1.00	1.25	1.28	1.38	1.11
102.5	1.17	1.24	1.22	1.34	1.65
115.0	1.24	1.21	1.20	1.56	1.39
128.0	1.12	1.23	0.69	1.24	1.19

TABLE 5
HST OBSERVATIONS

HST DATA SET	DATE	OBS TIME(UT)	FILTER	<i>exp_{avg}</i>	(Δ X)	(Δ Y)	P.A.
W00G0201/2T	15/09/91	00:10:39/01:31:39	F517N	598.75s	2.60	-0.32	90.499 ^o
W00G0203/4T	15/09/91	03:04:39/03:17:39	F547M	304.50s	2.60	-0.32	90.499 ^o
W00G0101/2T	14/09/91	01:37:39/02:58:39	F517N	559.00s	0.00	0.00	91.357 ^o
W00G0103/4T	14/09/91	04:31:39/04:44:39	F547M	352.25s	0.00	0.00	91.357 ^o
W00G0301/2T	12/09/91	19:01:39/22:22:39	F517N	413.50s	1.25	-2.20	92.515 ^o
W00G0303/4T	12/09/91	21:55:39/22:08:39	F547M	400.00s	1.25	-2.20	92.515 ^o
W00G0401/2T	08/09/91	19:40:39/21:19:39	F517N	600.00s	1.70	1.20	68.280 ^o
W00G0403/4T	08/09/91	22:56:39/23:09:39	F547M	287.75s	1.70	1.20	68.280 ^o
W11Z0101/2T	20/09/92	05:47:38/07:23:38	F648M	1922.50s	0.00	0.00	94.030 ^o
W11Z0103/4T	20/09/92	08:34:38/09:06:38	F718M	893.50s	0.00	0.00	94.030 ^o
W11Z0105/6T	20/09/92	10:34:38/12:10:38	F648M	1900.00s	0.00	0.00	94.030 ^o
W11Z0107/8T	20/09/92	13:32:38/13:55:38	F718M	1000.00s0	0.00	0.00	94.030 ^o

Pictor A – Simkin, Sadler, Sault, Tingay and Callcut

Figure 1 (a) Continuum image centered on 6560Å. Contours are logarithmic starting at 1% of peak intensity. (b) H α image; gray scale display is the square root of the relative intensity with a lower limit at 0.1% of peak intensity.

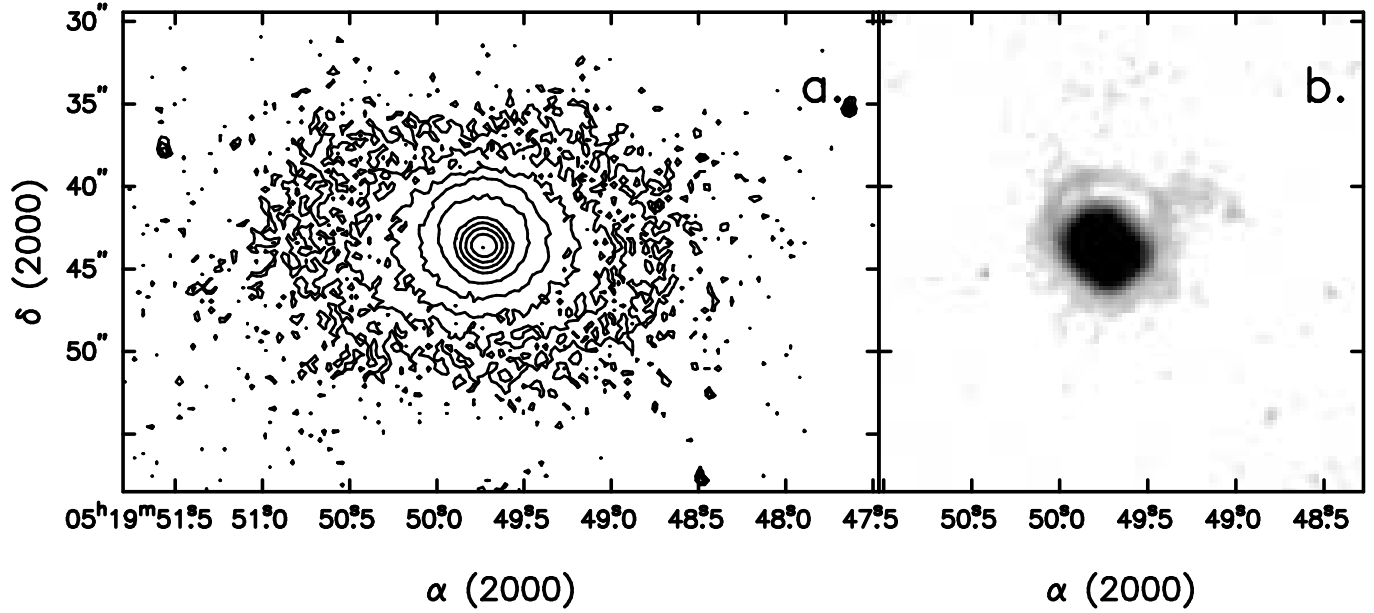


Figure 2 The 1.5 GHz VLA radio continuum map of . The inset shows the faint, inner part of the jet, with isophotes of the ground-based H α image superimposed. The two arrows indicate the direction of the NW hotspot at \sim PA 280 $^\circ$ and the counter direction to the SE hotspot at \sim PA 290 $^\circ$.

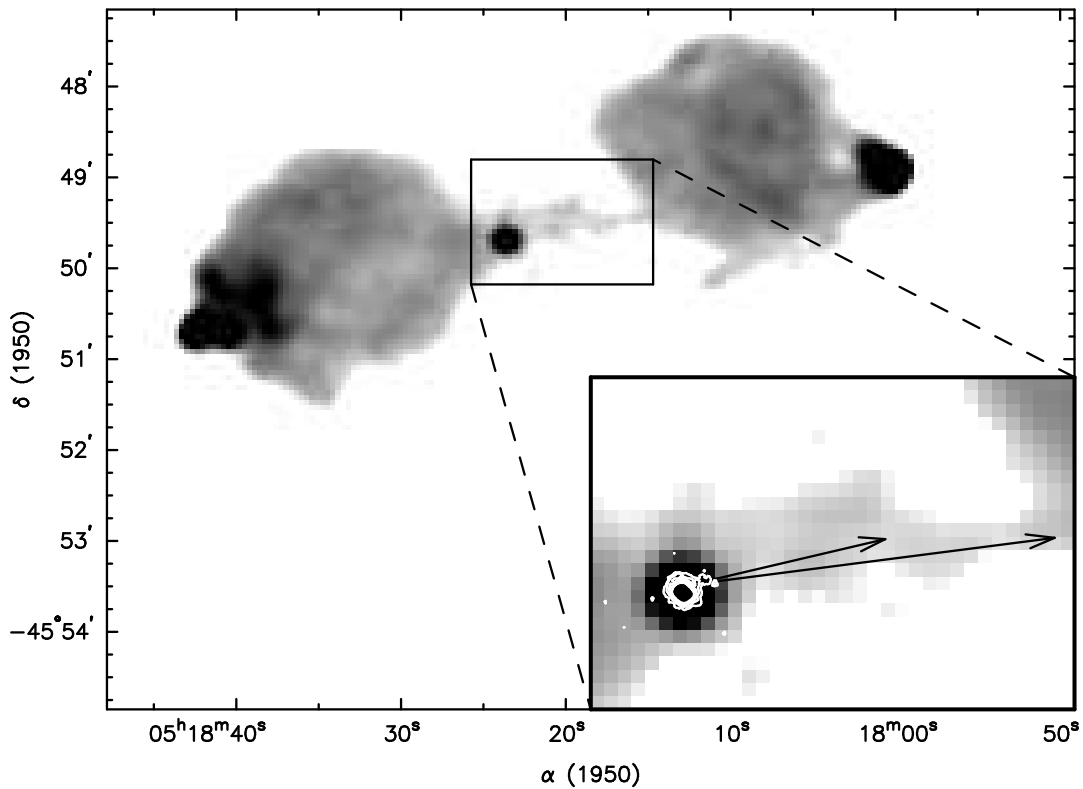


Figure 3. The ATCA 3cm image, the linear gray-scale ranges from $450 \mu\text{Jy}$ to 400 mJy . Inset shows isophotes of the radio nucleus superimposed on the ground-based $H\alpha$ image (from Fig 1b). The arc or loop in the 3 cm emission at a peak brightness which is 10% of the core source appears to lie inside the gap between the $H\alpha$ loop to the north and the main body of ionized H II around the nucleus - see discussion in Section 2.2.3. .

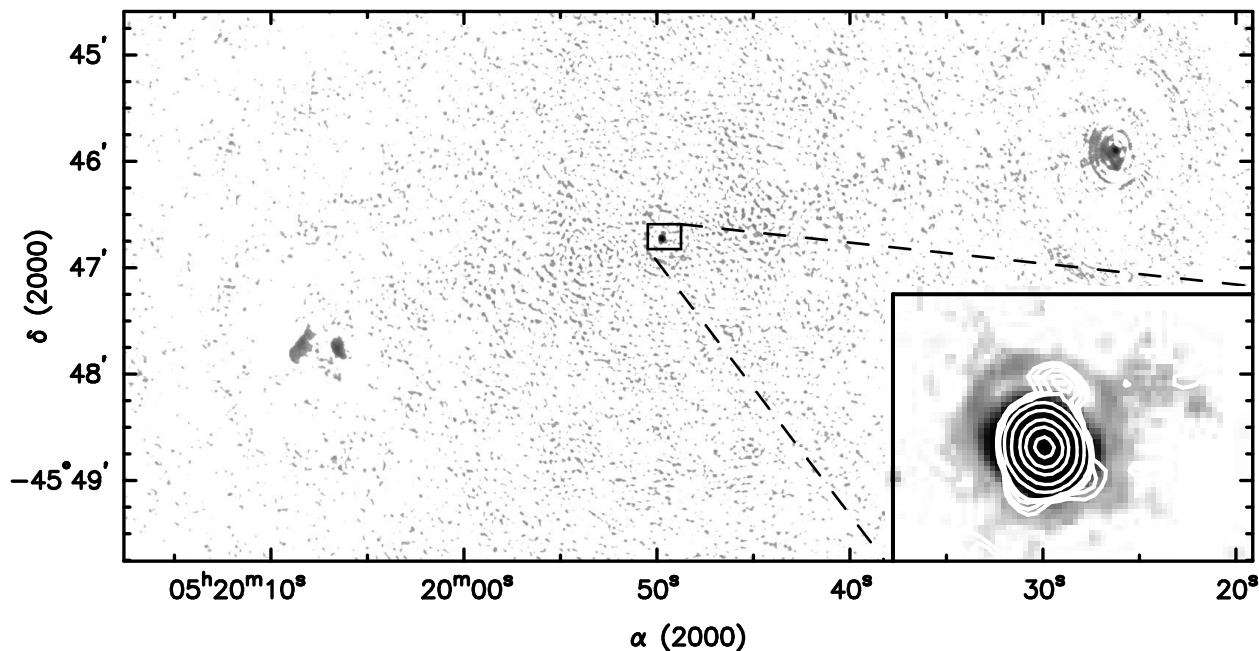


Figure 4. a-b Mean velocity cuts through indicated position angles. Left side: measured velocity, Right side: normalized to nuclear velocity.

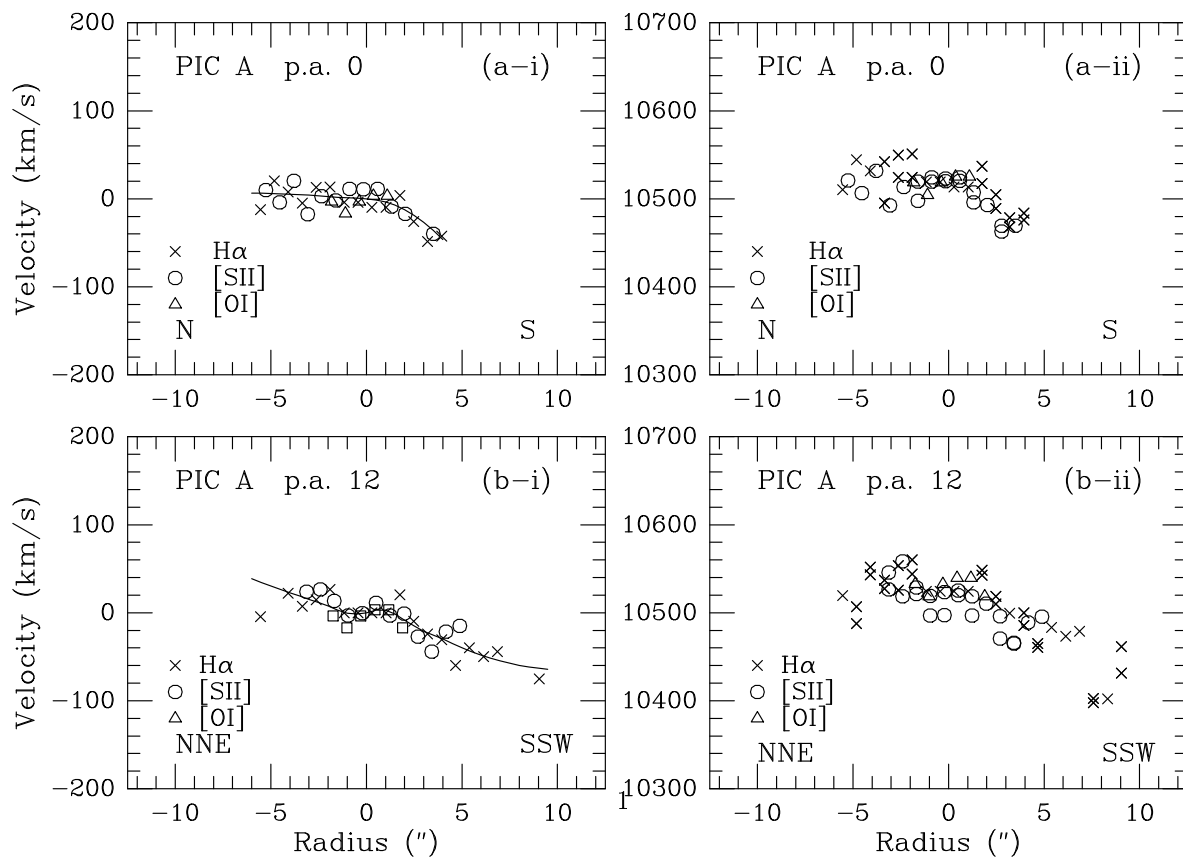


Figure 4. c-d Mean velocity cuts through indicated position angles. Left side: measured velocity, Right side: normalized to nuclear velocity.

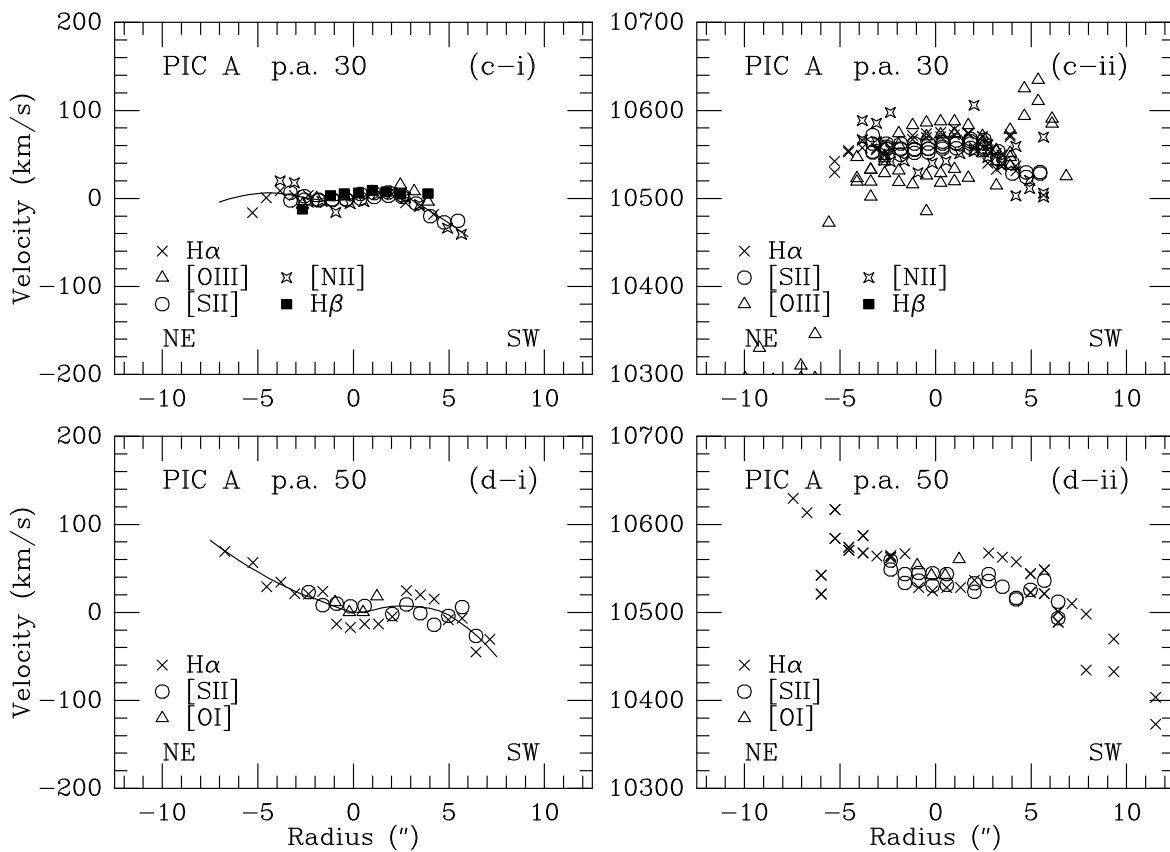


Figure 4. e-f Mean velocity cuts through indicated position angles. Left side: measured velocity, Right side: normalized to nuclear velocity.

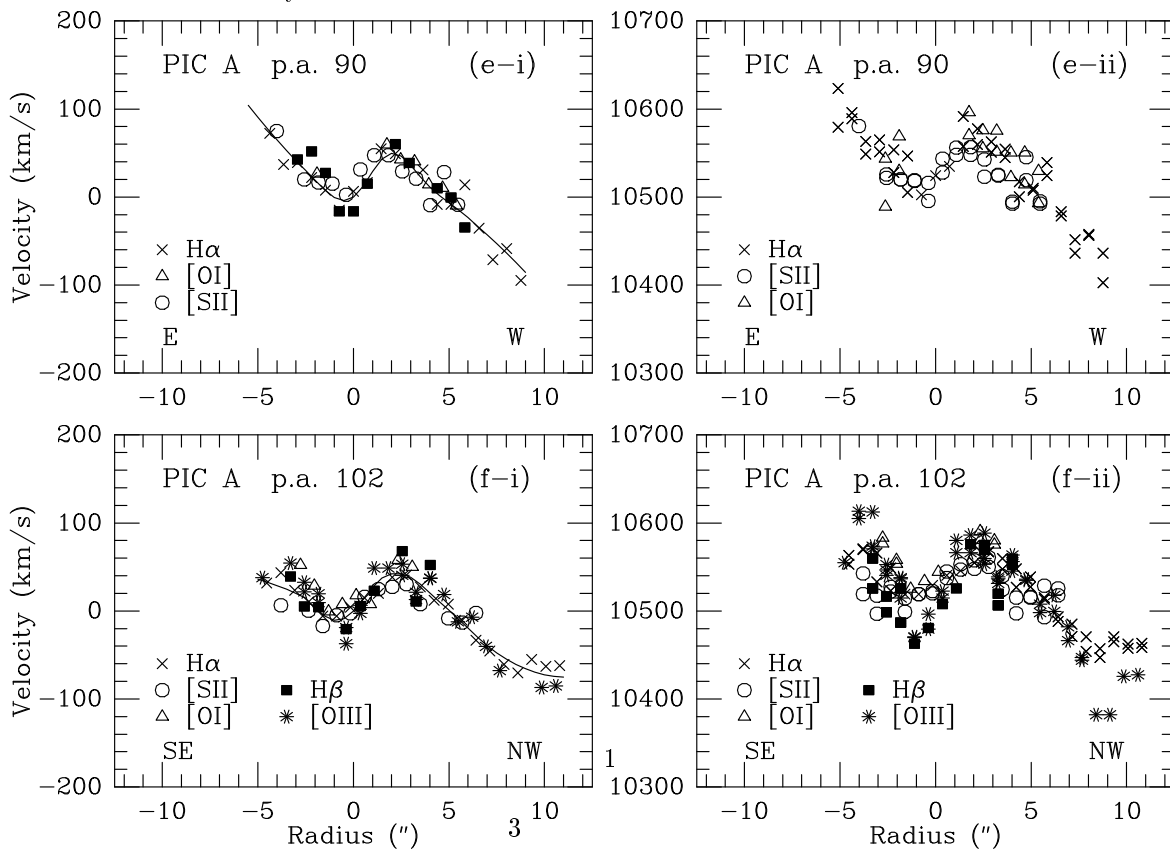


Figure 4. g-h Mean velocity cuts through indicated position angles. Left side: measured velocity, Right side: normalized to nuclear velocity.

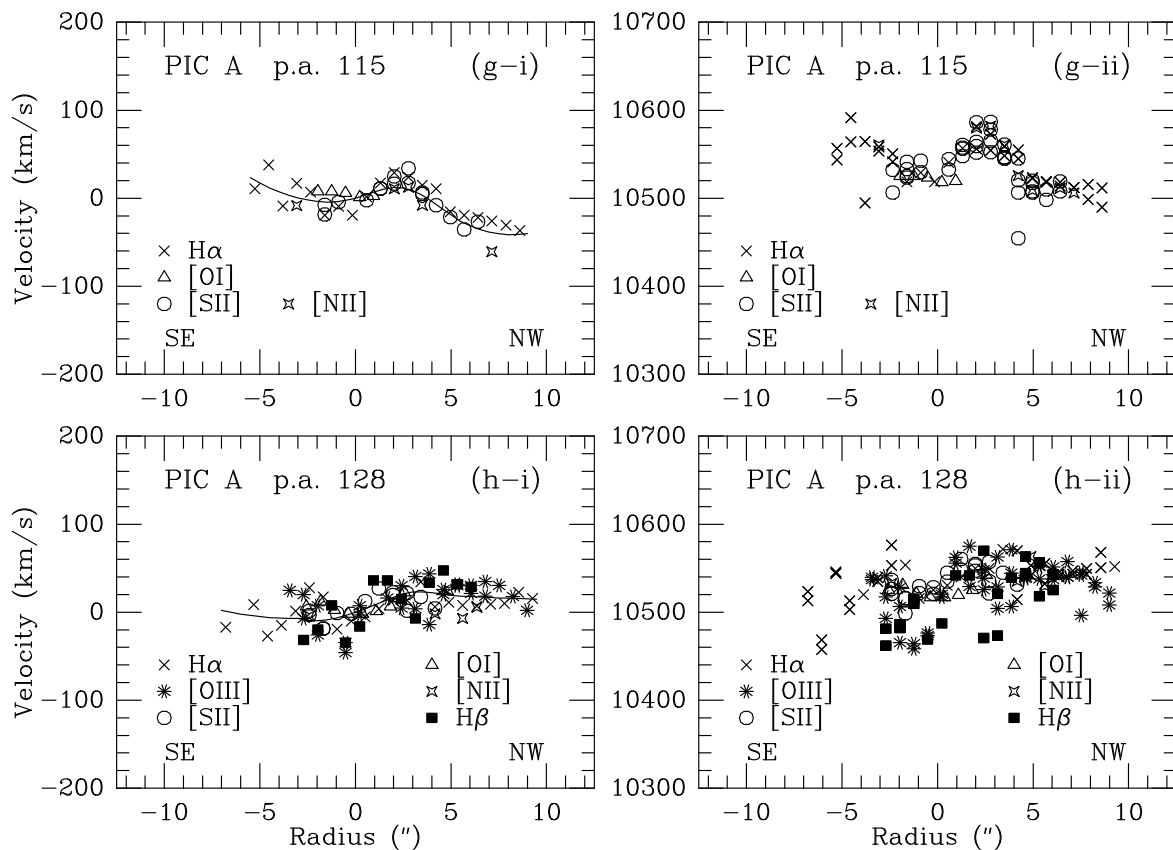


Figure 5 (a) Optical continuum image (from Fig. 1a), with slit positions superimposed. (b) Velocity map, superimposed on center of the H α image (1b). Velocity range is -70 to +100 km s^{-1} with negative velocities shown as dotted lines.

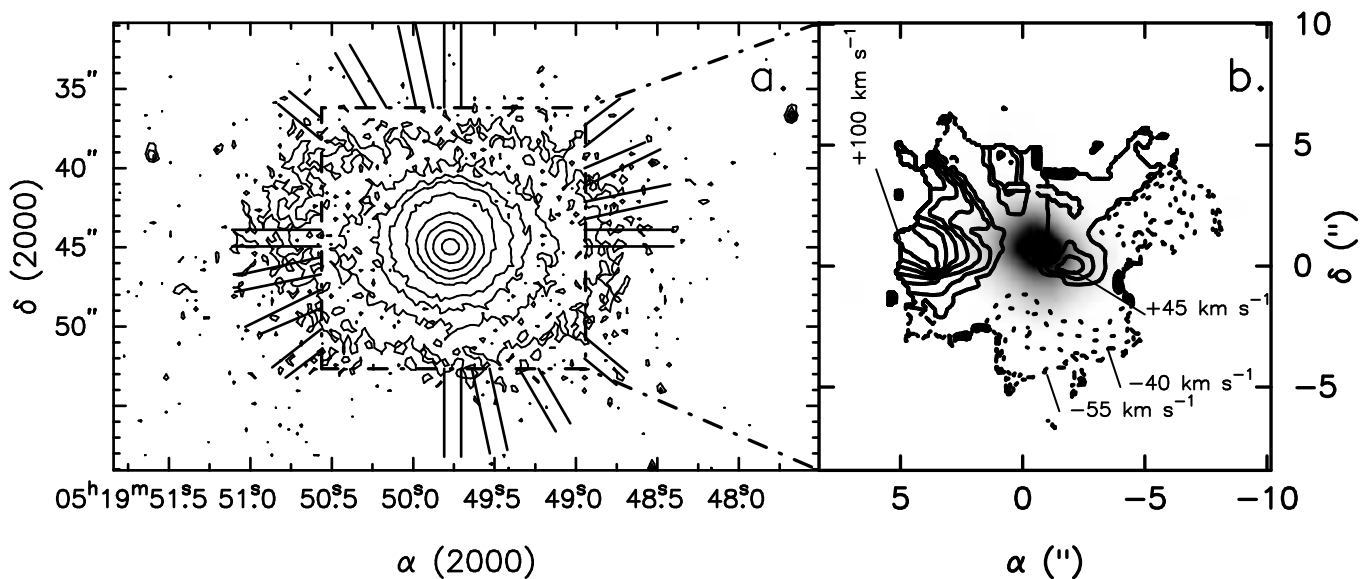


Figure 6. The $H\alpha$ -[NII] region of the optical spectrum in PA 102° for successive cuts through the galaxy in the region of the redshifted velocity component seen in Fig 5¹. The relative intensities have been scaled (see text). The inset shows the full nuclear spectrum for comparison.

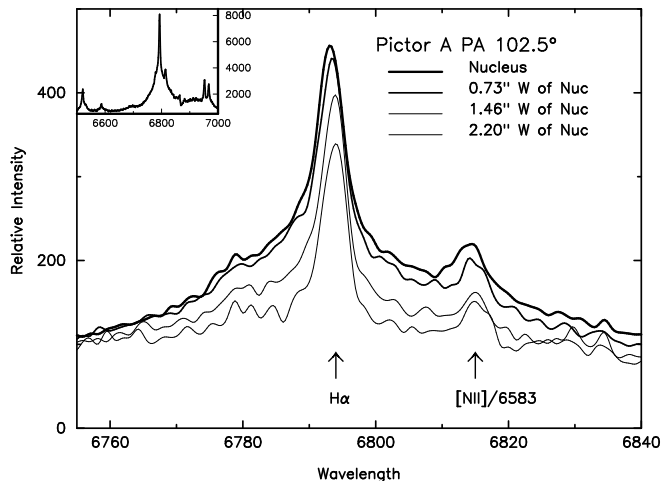
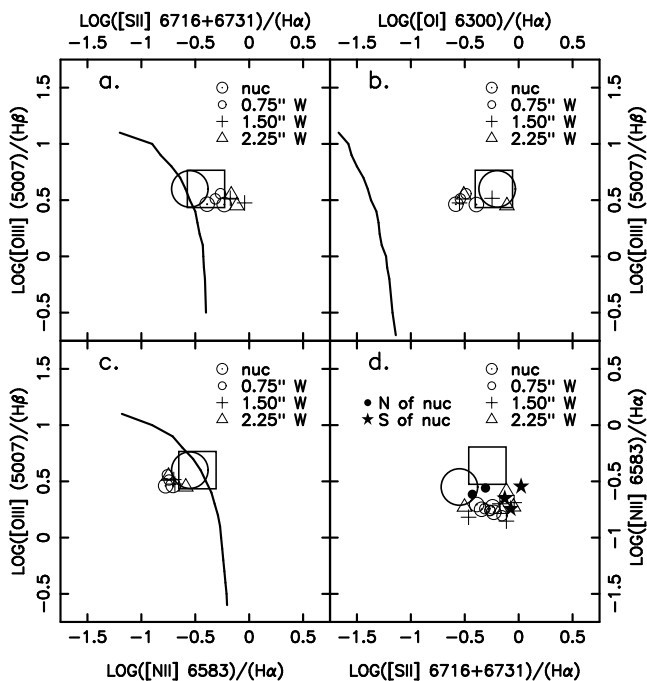


Figure 7. Line diagnostic diagrams (“BPT” diagrams Baldwin *et al.* (1981), Veilleux and Osterbrock (1987)). The large symbols (circle and square) mark the positions of one of the “dusty abundance” models and one of the “solar abundance” models by Ferguson *et al.* (1997). The solid curves, taken from Veilleux and Osterbrock (1987), mark the division between HII region like objects and narrow emission-line galaxies. (see text.)



REFERENCES

This 2-column preprint was prepared with the AAS L^AT_EX macros v4.0.

Figure 8. (a) Schematic composite of 4 “dithered” images. (b) Actual shift and orientation of the four HST Cycle 1 images of Pictor A.

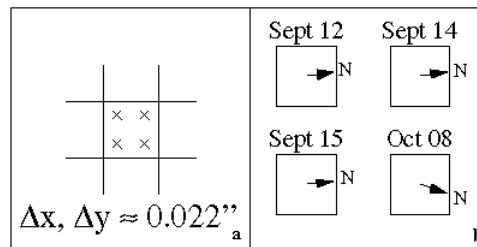


Figure 9. (a) Observed PSF F517N. (b) Calculated PSF F517N. (c) (a) divided by (b).

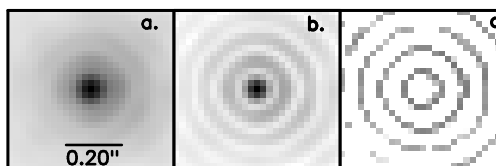


Figure 10. Reduced Cycle 1 HST “continuum” images. Grayscale with contours superimposed. The lower contours are 5, 10, 20 and 40 times the measured rms in the image. The upper contours are 90 60 30 15 and 7.5% of the peak. (a) and (c) are the F547M image deconvolved using (a) an observed PSF and (c) one generated by the STSDAS “tiny tim” software; (c) and (d) are images (a) and (b) corrected for [OIII] emission. The arrows in (c) and (d) point towards the center of the NE hotspot (lower arrow) and the anti-center of the SW hotspot (upper arrow) respectively.

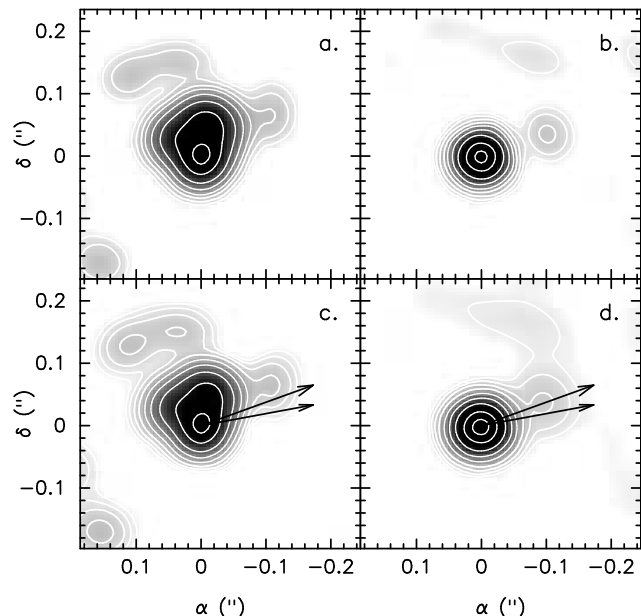


Figure 11. Reduced Cycle 1 HST “[OIII]” images. Grayscale with contours superimposed. The lower contours are 5, 10, 20 and 40 times the measured rms in the image. The upper contours are 90 60 30 15 and 7.5% of the peak. (a) and (b) Show the F517N image deconvolved using an observed PSF, The contours in (a) are from the image in Fig 10a. (c) is image (b) corrected for continuum and (d) shows the F517N image deconvolved using a “Tim” PSF after correction for continuum (see text)

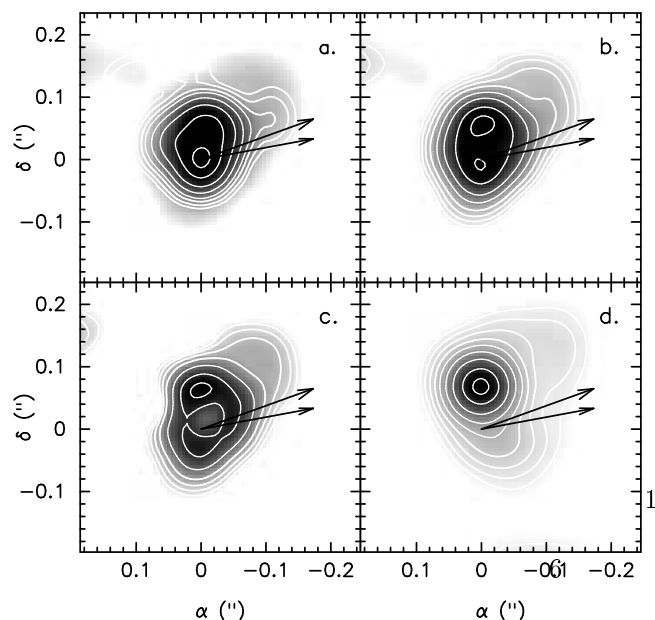


Figure 12. HST Cycle 2 images taken through the F648M filter. Grayscale with contours superimposed. The lower contours are 5, 10, 20 and 40 times the measured rms in the image. The upper contours are 90 60 30 15 and 7.5% of the peak. (a) has been deconvolved using a “Tim” profile. Note the different scales on (a) and (b). (see text).

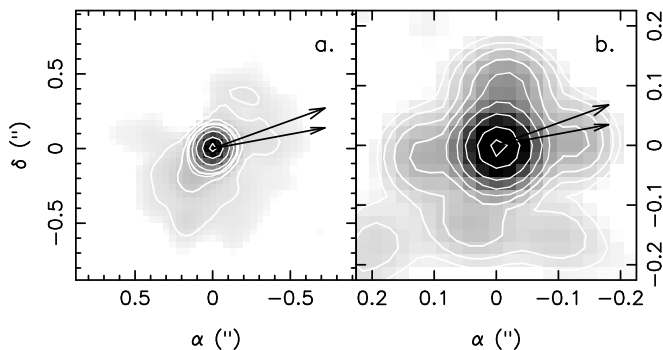


Figure 13. HST Cycle 2 continuum image with the VLBI jet superimposed. Lower optical contours are 6 12 and 18 times the measured rms in the image. Grayscale lower limit is 5mJy/beam (8.4 GHz, Beam FWHM 1.9×1.6 mas at $-8.6.^{\circ}$) (see text).

